

Wall slip and bulk yielding in soft particle suspensions

Gerhard Jung^{1,2,3} and Suzanne M. Fielding³

¹*Institut für Theoretische Physik, Leopold-Franzens-Universität Innsbruck, Technikerstraße 21A, A-6020 Innsbruck, Austria*

²*Institut für Physik, Johannes Gutenberg-Universität Mainz, Staudingerweg 9, 55128 Mainz, Germany*

³*Department of Physics, Durham University, Science Laboratories, South Road, Durham DH1 3LE, UK*

We simulate a dense athermal suspension of soft particles sheared between hard walls of a prescribed roughness profile, using a method that fully accounts for the fluid mechanics of the solvent between the particles, and between the particles and the walls, as well as for the solid mechanics of changes in the particle shapes. We thus capture the widely observed phenomenon of elastohydrodynamic wall slip, in which the soft particles become deformed in shear and lift away from the wall slightly, leaving behind a thin lubricating solvent layer of high shear. For imposed stresses below the material's bulk yield stress, we show the observed wall slip to be dominated by this thin solvent layer. At higher stresses, it is augmented by an additional contribution arising from a fluidisation of the first few layers of particles near the wall. By systematically varying the roughness of the walls, we quantify a suppression of slip with increasing wall roughness. For smooth walls, slip radically changes the steady state bulk flow curve of shear stress as a function of shear rate, by conferring a branch of apparent (slip-induced) flow even for $\sigma < \sigma_y$, as seen experimentally. We also elucidate the effects of slip on the *dynamics* of yielding following the imposition of a constant shear stress, characterising the timescales at which bulk yielding arises, and at which slip first sets in.

Concentrated suspensions of soft particles, such as microgels [1], emulsions [2], surfactant vesicles [3], block copolymer micelles [4], and multi-arm star polymers [5], display both solid and liquid rheological (deformation and flow) properties. Given an imposed shear stress lower than some yield stress, $\sigma < \sigma_y$, they typically show a solid-like creep response in which the shear strain γ slowly increases over time t , but with an ever decreasing shear rate, $\dot{\gamma} \sim t^{-\alpha}$. For a larger imposed stress, $\sigma > \sigma_y$, an early-time creep regime is followed, after a time that is often fit to the form $\tau_y \propto (\sigma - \sigma_y)^{-\delta}$ [6], by a yielding transition to a fluidised state of steady flow with a time-independent shear rate $\dot{\gamma}$, in which $\sigma(\dot{\gamma})$ is often fit to the 'Herschel-Bulkley' form $\sigma = \sigma_y + k\dot{\gamma}^n$, with $n \leq 1$ [7]. During yielding, the shear field within the fluid bulk often becomes highly heterogeneous [6, 8].

The motion of such materials is determined not only by their bulk properties, however, but also by their interaction with the confining walls. For smooth enough walls, a material will often appear to slip relative to them [9–13]: the velocity profile $v(y)$ across a sheared sample does not meet up with the velocity of the walls, but has an apparent mismatch known as the slip velocity, V_s . This has been suggested to arise via so-called elastohydrodynamic lubrication [14], in which soft particles become deformed by shear and lift away from the wall, leaving a thin lubricating solvent layer across which a strong shear occurs, giving apparent slip. (The hydrodynamic no-slip condition is however finally obeyed where the solvent meets the wall.) This is thought to be key to numerous processes in nature and technology, e.g., water-lubricated transport [15], food transport in the gut [16], and the squeezing of red blood cells through capillaries [17].

A series of remarkable experiments have shown wall slip to have a major impact on rheological data, which must be carefully interpreted to disentangle the contributions of bulk flow and slip [18]. Indeed, slip radically

changes the steady state flow curve, $\sigma(\dot{\gamma})$, by causing a non-zero apparent flow branch even below the bulk yield stress, $\sigma < \sigma_y$ [14, 19]. The steady state slip velocity $V_s(\sigma)$ typically depends as a power law on σ or $\sigma - \sigma_y$ (below or above σ_y). The value and universality of the exponent remain controversial [14, 19–25], although recent work demonstrated a linear scaling if contact line effects are removed [26, 27]. Slip also profoundly influences the *dynamics* of yielding, during which a state of initially solid-like response gives way to a finally fluidised flow [6, 8, 28–34]. Indeed, yielding often appears to initiate via slip at the wall, before a fluidised band propagates across the bulk to finally fluidise the whole sample. The degree of slip is however strongly influenced by confinement [35, 36], wall roughness [23, 37] or chemical coating [20, 38–40], bringing the intriguing prospect of controlling bulk flows by tailoring the wall conditions.

Compared with this remarkable experimental progress, simulation has lagged far behind, despite its potentially central role in addressing experimentally controversial issues such as the scaling of V_s with σ , and the dependence of V_s on features such as wall roughness, which is only rarely varied systematically in experiment [23].

The contributions of this Letter are fourfold. First, we introduce a method of simulating a dense suspension of soft particles sheared between hard walls of any prescribed roughness profile. It accounts fully for the fluid mechanics of the solvent between the particles, and near the walls, and for the solid mechanics via which the soft particles change shape. It is thus capable of properly capturing elastohydrodynamic slip. (Most existing methods instead simply assume a spherical interparticle potential and an effective solvent drag, although more advanced methods also exist [1].) Second, we quantify the effects of slip on steady state flow behaviour, confirming that it radically changes a material's flow curve $\sigma(\dot{\gamma})$ by conferring a branch of slip-induced apparent flow even for

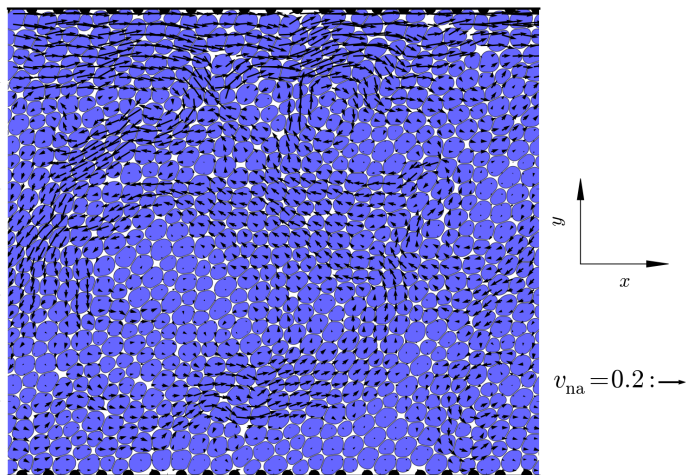


FIG. 1. Simulation snapshot at time $t = 17.5$, as the sample yields. Soft particles (blue), inter-particle fluid (white), rough hard walls (black). Arrows show non-affine velocity field v_{na} . Wall roughness $\beta = 0.59$, imposed stress $\sigma = 0.5$.

$\sigma < \sigma_y$. We show that the steady state slip velocity $V_s = \nu(\beta)(\sigma - \sigma_y)$ for $\sigma > \sigma_y$, with a transition in which the prefactor ν drops sharply above a critical wall roughness β^* , suppressing slip. For $\sigma < \sigma_y$, we separately find $V_s \propto \sigma$ with smooth walls. Below yield, slip is indeed dominated by a thin Newtonian layer at the wall, consistent with a picture of elasto-hydrodynamic slip. In important contrast, however, above yield it additionally includes a fluidisation of the first few layers of particles. Third, we elucidate the effects of slip on the *dynamics* of yielding following the imposition of a constant stress, characterising the timescales $\tau_y(\sigma)$ at which bulk yielding arises, and $\tau_s(\sigma, \beta)$ at which slip first sets in as a material starts to flow. Finally, we show that slip and bulk effects can be disentangled, with master creep and flow curves for the fluid bulk, regardless of wall roughness.

Our simulation method is summarised as follows (see Appendix A for details). We first initialise a two-dimensional packing of particles by equilibrating a bidisperse ensemble of particles of modest area fraction, with a simple spherical soft inter-particle potential. We then discretise the perimeter of each particle into nodes, invoking soft elastic interactions between neighbouring nodes on the same particle, and Lennard-Jones (LJ) interactions between the nodes of neighbouring particles. The particles are then blown up via an internal pressure, with the interactions just described capturing perimeter particle shape changes. We finally shear the packing via an immersed boundary method [41], which models the elastic particle perimeters as Lagrangian meshes that move over a fixed Eulerian mesh, on which we solve the Stokes equation, thereby implementing full hydrodynamics. The rough walls are also modelled as immersed boundaries, with LJ interactions between wall and particle nodes. A sample particle packing is shown in Fig. 1.

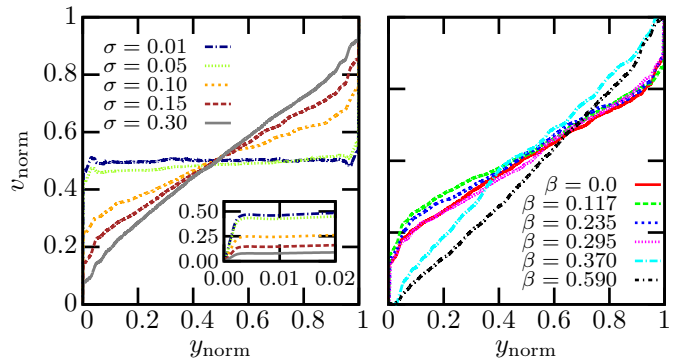


FIG. 2. Steady state velocity profiles. **Left**): at several shear stresses for smooth walls, $\beta = 0.0$. Inset: zoom near wall. **Right**): several wall roughnesses at shear stress $\sigma = 0.15$.

The simulation parameters are as follows: the height of the simulation box, $L_y = 1.0$ (length unit); the height of the channel containing the sheared soft particles, $H = 0.44$ (the space of height $L_y - H$ outside the channel contains only Newtonian solvent); the channel length, $L_x = 0.5$; the radius, b , and separation, B , of the wall bumps, which we keep in fixed ratio $B/b = 5.0$ across all runs; the number of soft particles $N = 800$; the particle boundary elastic constant $K_e = 1.0$ (stress unit); the wall elastic constant $K_{wall} = 20000.0$; the solvent viscosity $\eta = 1.0$ (viscosity unit); the LJ parameters between nodes of neighbouring particles; and the numerical timestep and mesh parameters (see Appendix A for details). The particle area fraction is fixed at $\phi = 0.84$ (giving the average particle radius $R = 0.0085$). Combined with the repulsive part of the LJ potential, this ensures the packing is jammed at rest. Parameters to be explored are then the scaled wall roughness $\beta \equiv b/R$ and imposed shear stress σ .

We measure from our simulations the Lagrangian wall velocities V_{lower} and V_{upper} . The apparent shear rate across the channel is then $\dot{\gamma}_{wall} = (V_{upper} - V_{lower})/H$. This includes a contribution from true shear across the fluid bulk, and from a thin slip layer adjacent to each wall. To disentangle these contributions, we measure the flow speed in the main flow direction x at any location on the Eulerian grid between the walls as $v(x, y)$, and average it along x to get the velocity profile $\bar{v}(y)$ across the channel. Over a reduced gap that excludes the slip layers, from $y = y_{lower} + 5R$ to $y = y_{upper} - 5R$, we fit $\bar{v}(y)$ to a straight line, $v_{fit}(y)$. The slope of this line then gives the bulk shear rate $\dot{\gamma}_{bulk}$, and its wall intercepts give the slip velocities: $V_{s,lower} = v_{fit}(y = y_{lower}) - V_{lower}$ and $V_{s,upper} = V_{upper} - v_{fit}(y = y_{upper})$. We report the average slip velocity $V_s = (V_{s,lower} + V_{s,upper})/2$. We define the normalised velocity profile $v_{norm}(y) = (\bar{v}(y) - V_{lower})/(V_{upper} - V_{lower})$ versus $y_{norm}(y) = (y - y_{lower})/H$.

The steady state [42] normalised profiles (Fig. 2, left) reveal two separate contributions to the slip: one from a very thin solvent layer within about $\Delta y = 0.0025$ of

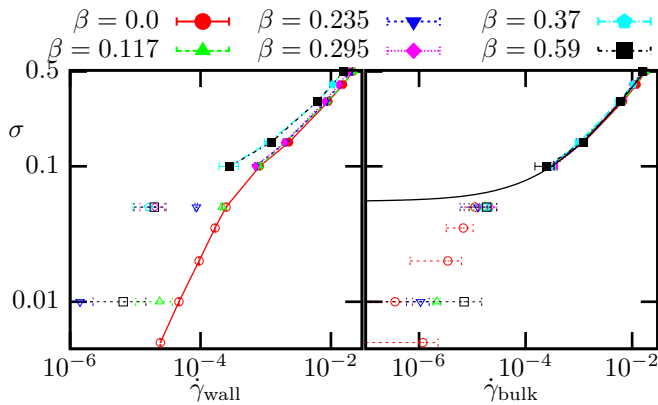


FIG. 3. **Left)** Apparent flow curves with shear rates calculated from relative wall speeds, including wall slip, for different wall roughnesses β . Solid line connects data points for smooth wall case. **Right)** Corresponding bulk flow curves using shear rate obtained from internal velocity profile, with slip removed. Filled symbols: steady state (errors bars too small to be seen at high stresses). Unfilled symbols: do not attain steady state, with dashed error bars showing drift during the time $t > 2000$ over which data is taken. Solid line: fit to $\sigma = \sigma_y + k\dot{\gamma}_{\text{bulk}}^n$ with $\sigma_y = 0.055 \pm 0.004$ and $n = 0.57 \pm 0.03$.

the wall (inset), and another over about $\Delta y = 0.1$, corresponding to an increase in fluidity over the first few particle layers near the wall [23, 43, 44]. Importantly, we find the first contribution to dominate the total slip at stresses below yield, whereas above yield both are important. We report the total slip, because it is more likely to be the one seen in experimental velocimetry of realistic pixel resolution. We note that $\bar{v}(y_{\text{lower}}) = V_{\text{lower}}$ (as seen in the inset) and $\bar{v}(y_{\text{upper}}) = V_{\text{upper}}$, consistent with hydrodynamic no-slip for the solvent.

Fig. 3 shows the steady state flow curve relationship between the imposed shear stress σ and the shear rate $\dot{\gamma}$, for several different values of the wall roughness parameter β . (Although in our simulations σ is imposed and $\dot{\gamma}$ measured, we show $\sigma(\dot{\gamma})$ because this is the usual flow-curve representation.) The left panel has as its abscissa the apparent shear rate, $\dot{\gamma}_{\text{wall}}$, defined via the relative wall speed. As noted above, this includes not only any true shear across the fluid bulk, but also the effects of wall slip. The right panel uses the true bulk shear rate, $\sigma(\dot{\gamma}_{\text{bulk}})$, with slip removed. Above a yield stress, $\sigma > \sigma_y$, the steady state data superpose for all levels of wall roughness, once slip is removed. The resulting flow curve is then fit to the Herschel-Bulkley form, $\sigma = \sigma_y + k\dot{\gamma}^n$, with $\sigma_y = 0.055 \pm 0.004$ and $n = 0.57 \pm 0.03$. For lower stresses, $\sigma < \sigma_y$, $\dot{\gamma}_{\text{bulk}}$ does not attain a steady state, as indicated by the open symbols in Fig. 3.

We now further explore the extent to which the flow profiles across the gap are heterogeneous due to wall slip and non-affine flows in the bulk. Fig. 4a) shows the steady state wall slip velocity as a function of imposed shear stress, for several levels of wall roughness, β . The data for $\sigma > \sigma_y$ are fit for each roughness to the form

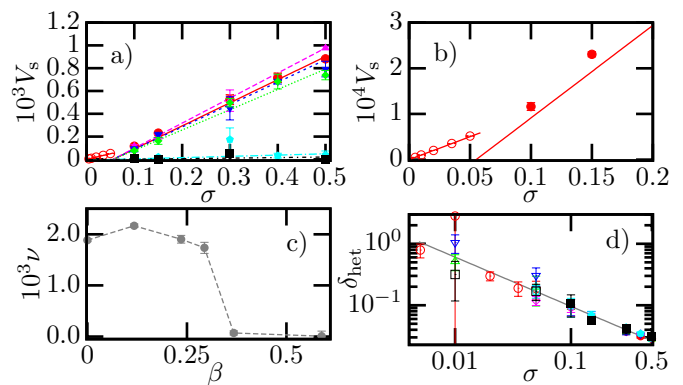


FIG. 4. **a)** Symbols: steady state slip velocity vs. imposed stress for different wall roughnesses, with roughness symbol legend as in Fig. 3. Lines: least-square fits to $V_s(\sigma > \sigma_y) = \nu(\beta)(\sigma - \sigma_y)$ and $V_s(\sigma < \sigma_y) = \nu_N(\beta)\sigma$. **b)**: Zoom of $\beta = 0.0$ data for $\sigma < 0.2$. **c)**: Prefactor ν vs. wall roughness β . **d)**: Steady state degree of heterogeneity in the bulk flow field vs. imposed stress for different surface roughnesses. Solid line: $\delta_{\text{het}} \propto \sigma^{-0.8}$ as a guide to the eye.

$V_s = \nu(\beta)(\sigma - \sigma_y)^p$, with $p = 1$. (We also find $p = 1$ with an essentially unchanged $\nu(\beta)$ if we instead allow a free intercept.) This linear dependence for $\sigma > \sigma_y$ is consistent with the experiments of Ref. [20, 26, 27] whereas those of Ref. [22, 24] found a quadratic dependence, $p = 2$. In Ref. [25], it was suggested that p varies between 1 and 2 as a function of packing fraction ϕ above jamming. It would be interesting in future to simulate a range of ϕ . The prefactor ν , plotted as a function of β in panel c), reveals a transition from strong slip for smooth walls, with $\beta < \beta^* \approx 0.3$, to suppressed slip for rougher walls, $\beta > \beta^*$. A decreasing slip with increasing wall roughness was seen for wall roughnesses less than the average particle size ($\beta < 1$) in Ref. [23].

For $\sigma < \sigma_y$, we find a different scaling of the slip velocity, $V_s \propto \sigma$, for smooth walls. (For rough walls, V_s takes prohibitively long to attain a steady state.) That we observe different scalings for $V_s(\sigma)$ above and below yield is consistent with the discussion above regarding Fig. 2, left: that slip below yield is dominated by a thin solvent layer at the wall, with an additional contribution above yield from fluidisation of the first few particle layers.

In addition to this apparent slip at the walls, the flow profile within the fluid bulk also shows strong departures from affine shear. This is already apparent in the snapshot of Fig. 1, in which the arrows show the degree to which the flow velocity at any location differs from a simple linear shear profile. In Fig. 4 we quantify the bulk flow heterogeneity (on average, in steady state) via the parameter δ_{het} [45], plotted as a function of the imposed stress for several different levels of wall roughness. This increases with decreasing imposed stress as $\delta_{\text{het}} \sim \sigma^{-0.8}$. It is relatively independent of wall roughness, showing that the effects of the wall persist only a few particle diameters into the bulk. This result suggests that the dy-

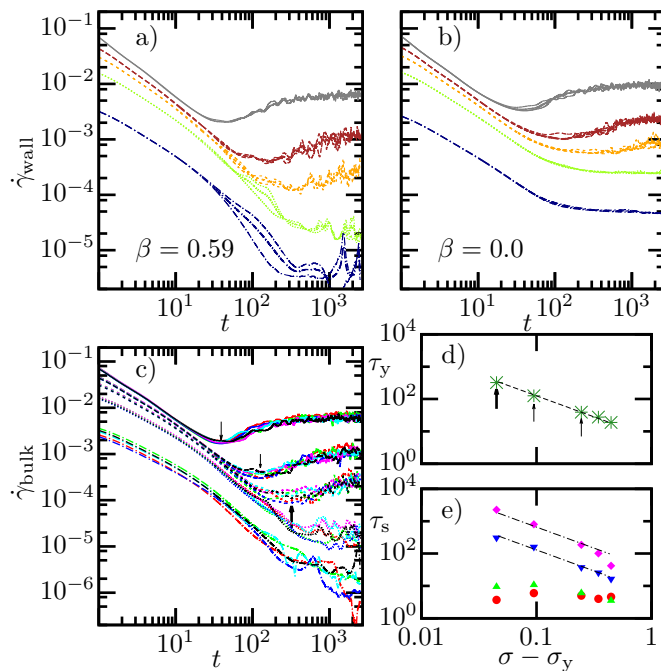


FIG. 5. Apparent shear rate vs. time for shear stresses $\sigma = 0.3, 0.15, 0.1, 0.05, 0.01$ in curve bundles downwards for (a) a rough wall and (b) a smooth wall. (In each bundle, thick line shows average over 2 or 4 runs; thin lines show individual runs.) (c) Corresponding true shear rate vs. time for the same imposed stresses. (In each bundle, curves are for several roughnesses, with colour code as in Fig. 3. For each roughness, curve is averaged over 2 or 4 runs.) (d) Yielding time τ_y at the minimum in $\dot{\gamma}_{\text{bulk}}(t)$ (averaged over roughnesses), as a function of stress above yield. Dotted line: power -1.3 . (Arrows denoting times in c) and d) coincide.) (e) Time τ_s at which wall slip velocity V_s attains half its steady state value for the 4 smoothest walls, with roughness symbols as in Fig. 3. Dot-dashed line: power -1.3 .

namical heterogeneity diverges at $\sigma \rightarrow 0$ under conditions of imposed stress, distinct from the divergent avalanche size seen at low imposed strain rate $\dot{\gamma} \rightarrow 0$ [46].

We now investigate the transient evolution as a function of the time t since the imposition of a constant stress σ on a sample that is freshly prepared then aged for a waiting time $t_w = 50.0$, before shearing starts at $t = 0$. In particular, we explore the dynamical yielding process via which a regime of initial creep, with a strain rate that decreases over time, gives way to a final steady state flow.

Figs. 5a,b) show the apparent shear rate (as measured via the relative wall speeds, and so including the effects of slip) as a function of time t for a rough wall (a) and smooth wall (b). In each case, data are shown for five imposed stress values in separate curve bundles. The highest three stress values are all above the yield stress, $\sigma > \sigma_y = 0.055$. Here, the apparent shear rate $\dot{\gamma}_{\text{wall}}$ initially decreases as function of time, before attaining a minimum. The sample then yields and the shear rate increases to attain a steady flowing state. For the two

lowest stress values, for which $\sigma < \sigma_y$, the apparent shear rate attains a steady state only for smooth walls. This is due to the confounding effects of slip: with rough walls, where slip is suppressed and $\dot{\gamma}_{\text{wall}}$ coincides with the true bulk shear rate $\dot{\gamma}_{\text{bulk}}$, the shear rate never attains a steady state but continues to slowly decrease.

For the same five values of stress, the true bulk shear rate is shown as a function of time in Fig. 5c). The curve bundle for each stress value now shows results for the six values of wall roughness explored in the flow curves of Fig. 3. Now that the effects of wall slip have been removed by plotting $\dot{\gamma}_{\text{bulk}}(t)$, the data for all wall roughnesses essentially coincide. In this way, we find the yielding dynamics in the fluid bulk to be largely independent of wall roughness. We extract by eye the time at the minimum in $\dot{\gamma}_{\text{bulk}}$ and define this to be the time τ_y at which yielding occurs. This shows a good fit to $\tau \sim (\sigma - \sigma_y)^{-1.3}$ (Fig. 5d). Similarly, we determine the time τ_s at which slip first arises at the wall (defined as the time at which $V_s(t)$ attains half its steady state value). We plot this as a function of $\sigma - \sigma_y$ in Fig. 5e) for the four lowest values of wall roughness explored in the flow curves of Fig. 3. (For the two roughest walls in Fig. 3, no appreciable slip arises.) This slip timescale increases with increasing wall roughness. For the largest two roughness values at which slip occurs, τ_s further appears to depend on stress in the same way as the timescale for bulk yielding, with $\tau_s \sim (\sigma - \sigma_y)^{-1.3}$. Whether slip pre-empts bulk yielding (or vice versa), as determined by the prefactor, however depends on the roughness.

To summarise, we have introduced a method for simulating the dynamics of a dense athermal suspension of soft particles sheared between hard walls of any roughness profile, in order to study the key rheological phenomenon of wall slip. For imposed stresses below the bulk yield stress, we have shown wall slip to be dominated by a thin solvent layer adjacent to the wall. In contrast, for imposed stresses above yield we find an additional slip contribution arising from a fluidisation of the first few particles layers. We have further characterised the scaling of slip velocity with imposed stress, and demonstrated a transition from strong to suppressed slip with increasing wall roughness. We have also characterised the dependence of the timescale for yielding within the bulk fluid on the imposed stress, and of the timescale for slipping at the wall as a function of both imposed stress and wall roughness. In future, it would be interesting to study slip in less concentrated soft suspensions, below jamming; rougher wall profiles to address a return of slip for roughnesses exceeding the particle diameter [23]; and different interaction potentials with the wall.

Since this manuscript was written, we have become aware of a manuscript studying the effects of wall slip on a dense suspension of droplets in steady state pressure driven flow along a channel [47]. It focuses entirely on steady state behaviour, presenting results for the mass throughput along the channel as a function of wall shear stress and wall roughness.

Acknowledgements — We thank Thibaut Divoux for discussions. This work was funded by the Deutsche Forschungsgemeinschaft (DFG, German Research Foundation) - Project number 233630050 - TRR 146.

Appendix A: Simulation method

We now introduce our method for simulating a two-dimensional dense suspension of soft particles, sheared between hard walls of any prescribed roughness profile.

1. Initialization

a. Molecular dynamics of circular particles

We take a box of length L_x and height L_y with periodic boundaries in x and y . Inside the box we randomly initialise an ensemble of $p = 1 \dots P$ circular particles in a region of length L_x and height $H - b$ with packing fraction $\phi = 0.5$. (In the next stage, the particles will be expanded to attain a higher ϕ .) To avoid crystallisation we take a bidisperse 50:50 mixture with particle radii in ratio 1 : 1.4. Particles closer than a distance $r_{c,pp'}$ interact *via* a Lennard-Jones (LJ) potential:

$$\mathbf{F}_p^{\text{LJ}} = -\nabla_p E^{\text{LJ}}(\{\mathbf{X}_{p'}\}), \quad (\text{A1})$$

$$E^{\text{LJ}}(\{\mathbf{X}_{p'}\}) = 4K_{\text{LJ}} \sum_{p,p' < p} \left[\left(\frac{\sigma_{pp'}}{X_{pp'}} \right)^{12} - \left(\frac{\sigma_{pp'}}{X_{pp'}} \right)^6 \right]. \quad (\text{A2})$$

Here \mathbf{X}_p is the position of the p th particle, $X_{pp'} = |\mathbf{X}_p - \mathbf{X}_{p'}|$ the distance between the p and p' th particles, K_{LJ} a force constant and $\sigma_{pp'}$ a length. Each particle also experiences dissipative drag and thermal noise, and accordingly obeys (subject to additive corrections from

Symbol	Parameter	Value
P	number of particles	800
L_y	box height	1.0 [length unit]
L_x	box width	0.5
ϕ	area packing fraction	0.5
M	particle mass	1.0 [mass unit]
K_{LJ}	LJ energy constant	1.0 [energy unit]
$\sigma_{pp'}$	LJ length constant (particle-particle)	$1.2(R_p + R_{p'})$
$r_{c,pp'}$	LJ cutoff length (particle-particle)	$\sqrt[6]{2}\sigma_{pp'}$
τ	Langevin time constant	0.01
T	temperature	0.1
Δt	numerical time step	5.42×10^{-6}
H	wall separation	0.44
b	wall bump radius	[varied]
B	wall bump separation	$5.0b$
$\sigma_{ps'}$	LJ length constant (particle-wall)	0.001125
$r_{c,ps'}$	LJ cutoff (particle-wall)	$\sqrt[6]{2}\sigma_{ps'}$

TABLE I. Parameter values in the molecular dynamics stage.

wall interactions to be described in the next paragraph) the equation of motion:

$$M \ddot{\mathbf{X}}_p = \mathbf{F}_p^{\text{LJ}} - \frac{M}{\tau} \dot{\mathbf{X}}_p + \mathbf{F}_p^R. \quad (\text{A3})$$

Here M is the particle mass, τ a time-constant and \mathbf{F}^R a delta-correlated random variable with zero mean and variance $\frac{k_B T M}{\Delta t \tau}$.

Parallel walls are placed above and below the particle packing a distance $\Delta y = H$ apart. Each comprises a flat line of length L_x , periodically interrupted by semicircular bumps of radius b and separation B , which protrude into the packing. Each wall is discretised into many (N_w) nodes (we shall return below to discuss the value of N_w), and each wall node is held in a fixed position. A short-ranged LJ force then additionally acts between the particles and wall nodes. This is of the form of Eqn. A2, with the particle labels p' augmented by wall node labels s' .

To remove particle-particle and particle-wall node overlaps, we first minimize the interaction energy using the Polak-Ribiere version of the conjugate gradient algorithm (provided by the LAMMPS package [48]). The equations of motion, Eqn. A3, are then temporally discretized using the Velocity-Verlet algorithm [49] and evolved using LAMMPS [48] [50] with a timestep Δt until the ensemble reaches a statistical steady state after a time $\tau_{\text{eq}} = 5000\Delta t$.

b. Particle expansion and shape change

After the molecular dynamics equilibration just described, the boundary of each (initially) circular particle is discretized into evenly distributed surface nodes, separated a distance (initially) of $\Delta s = 2\pi R/N_s$. (We therefore use two different values of N_s , in ratio 1 : 1.4, to ensure the same Δs for the two particle species.) The particle boundaries are then rendered elastic via a force

Symbol	Parameter	Value
N_{s1}	boundary nodes per smaller particle	250
K_e	particle boundary elastic constant	2.0 [$2 \times$ energy unit]
K_p	expansion force constant	0.5
σ_{ij}	LJ length constant	0.00125
$r_{c,ij}$	LJ cutoff	$\sqrt[6]{2}\sigma_{ij}$
K_{LJ}	LJ energy constant	0.01
γ	drag	1.0 [sets time unit]
Δt	numerical time step	1.125×10^{-6}

TABLE II. Parameters values in the particle expansion stage. Values for P , L_x , L_y , H , b , B , [length unit] as in Table. I.

acting between adjacent nodes round each boundary:

$$\begin{aligned} \mathbf{F}_s^{\text{elastic}} &= \frac{T_{s+1/2}\boldsymbol{\tau}_{s+1/2} - T_{s-1/2}\boldsymbol{\tau}_{s-1/2}}{\Delta s}, \\ \boldsymbol{\tau}_{s+1/2} &= \frac{\mathbf{X}_{s+1} - \mathbf{X}_s}{|\mathbf{X}_{s+1} - \mathbf{X}_s|}, \\ T_{s+1/2} &= K_e \left(\frac{|\mathbf{X}_{s+1} - \mathbf{X}_s|}{\Delta s} - 1 \right), \end{aligned} \quad (\text{A4})$$

with K_e a surface elastic force constant. The index $s = 0 \cdots N_s - 1$ runs over the nodes of any particle boundary, with periodic boundary conditions. For clarity we omit here the particle number label p . Note that the actual distance $|\mathbf{X}_{s+1} - \mathbf{X}_s|$ between any two nodes will change during the simulation, whereas the equilibrium distance remains constant and equal to Δs .

As noted above, parallel walls are located above and below the particle packing a distance $\Delta y = H$ apart. Each wall is discretised into N_w nodes, with neighbouring nodes separated by the same curvilinear distance Δs that (initially) separates neighbouring nodes in the particle boundaries. (Accordingly, the actual number N_w used in any simulation depends on the values of b and B .) The wall nodes remain fixed in position during this part of the simulation. As above, a short-ranged LJ force acts between the nodes of different particles, and between particle and wall nodes. This is of the form of Eqn. A2, with the particle labels p' augmented by node labels s' .

The particles are expanded by a pressure that acts inside each particle, modelled via a force of amplitude K_p acting on each boundary node along the outward normal:

$$\mathbf{F}_s^{\text{pressure}} = K_p(\boldsymbol{\tau}'_s \times \hat{\mathbf{z}}), \quad (\text{A5})$$

with centred tangent $\boldsymbol{\tau}'_s = (\mathbf{X}_{s-1} - \mathbf{X}_{s+1})/|\mathbf{X}_{s-1} - \mathbf{X}_{s+1}|$. The boundary and wall nodes move as $\dot{\mathbf{X}}_s = \mathbf{F}_s/\gamma$, where \mathbf{F}_s is the total force on any node, against a drag γ , without explicit hydrodynamics in this initialisation phase. This equation is evolved using the explicit Euler algorithm with timestep Δt . As they expand, the particles change shape due to crowding, but avoid overlap via the short-ranged LJ potential. The wall shapes remain constant, with particle-wall overlaps also avoided by the LJ potential. The simulation is stopped when the desired area fraction is achieved.

2. Shearing with hydrodynamics

The configuration of particle boundary and wall nodes attained at the end of the initialisation procedure just described is then transferred to form the initial configuration in a code that now also incorporates shearing and hydrodynamics. In this hydrodynamic code, the Lagrangian particle boundary and wall nodes move relative to a fixed rectangular Eulerian mesh, on which we implement incompressible Stokes flow. The combined Eulerian and Lagrangian dynamics are handled using an

“immersed boundary method” [51]. At any timestep, this comprises the following substeps:

1. Given the source forces arising from the current configuration of particle boundary and wall nodes, as mapped onto the Eulerian mesh in step 5 of the previous timestep, the Stokes equation is solved to find the fluid velocity on the Eulerian mesh.
2. This Eulerian velocity field is mapped onto the Lagrangian particle boundary and wall nodes.
3. Using these Lagrangian velocities, the Lagrangian positions of the particle boundary nodes are updated. From these new positions, the new Lagrangian forces of the particle boundary nodes are calculated.
4. Again using the Lagrangian velocities from step 2, the Lagrangian positions and forces of the wall boundary nodes are updated.
5. These forces on the Lagrangian particle boundary and wall nodes are mapped to the Eulerian mesh.

Each substep is detailed in the correspondingly numbered subsection below.

At the start of the shearing simulation, we set the desired equilibrium distance Δs between adjacent boundary nodes of each particle to be equal to L/N_s , where L is the perimeter of a circle with the same area as that particle. This desired equilibrium distance then remains constant during the shearing simulation that follows. Additionally, the wall nodes are initialised with forces $\mathbf{F}_s = (+\sigma L_x/(N_w \Delta s), 0)$ and $(-\sigma L_x/(N_w \Delta s), 0)$ on the upper and lower walls respectively, to impose a shear stress on the soft particle suspension. The algorithm that follows then keeps this shear stress constant over the course of the simulation.

a. Stokes flow on the Eulerian mesh

We consider a biperiodic plane of size $L_x \times L_y$ in which are located Lagrangian walls a distance $\Delta y = H$ apart.

Symbol	Parameter	Value
η	solvent viscosity	1.0 [viscosity unit]
K_e	particle surface elastic constant	1.0 [stress unit]
ϕ	particle area fraction	0.84
R	average particle radius	0.0085
σ	LJ length constant	9dx
r_c	LJ cutoff	σ
K_{LJ}	LJ energy constant	10^{-9}
N_x, N_y	number of Eulerian grid points	4096 L_x , 8192 L_y
$\alpha = \Delta s/dx$	Lagrangian/Eulerian grid ratio	1.42
K_w	wall elastic constant	20000
Δt	numerical time step	0.002

TABLE III. Parameters used in shearing stage. Values for P , L_x , L_y [length unit], H , B , b , N_s , as in Table. II and/or I.

These will move relative to each other in order to perform shear. In the gap of size H are soft particles and a Newtonian solvent of viscosity η . In the complementary gap of size $L_y - H$ there is Newtonian solvent only. Over the full $L_x \times L_y$ plane, the fluid velocity field $\mathbf{v}(\mathbf{x}, t)$ and pressure field $p(\mathbf{x}, t)$ obey the incompressible Stokes equations:

$$0 = \eta \nabla^2 \mathbf{v} + \mathbf{f} - \nabla p, \quad (\text{A6})$$

$$0 = \nabla \cdot \mathbf{v}. \quad (\text{A7})$$

Here $\mathbf{f}(\mathbf{x}, t)$ is a source force density field, which acts only at the walls of the shearing cell, and round the boundaries of the soft particles. These Stokes equations are discretized on a fixed rectangular Eulerian mesh of $i = 0 \cdots N_x - 1, j = 0 \cdots N_y - 1$ points, with the same mesh size $dx = L_y/N_y = L_x/N_x$ in both x and y . (We describe below how to map the wall and particle boundary Lagrangian forces onto this Eulerian mesh.) The discretized differential operator is defined as:

$$D_x \phi_{i,j} = \frac{\phi_{i+1,j} - \phi_{i-1,j}}{2 dx}, \quad (\text{A8})$$

for any discretized field $\phi_{i,j}$, with $D_y \phi_{i,j}$ defined similarly. The discretized Stokes equations are then:

$$0 = \eta \mathcal{D}^2 \mathbf{u}_{i,j} + \mathbf{f}_{i,j} - \mathbf{D} p_{i,j}, \quad (\text{A9})$$

$$0 = \mathbf{D} \cdot \mathbf{u}_{i,j}, \quad (\text{A10})$$

with $\mathbf{D} = (D_x, D_y, 0)^T$ and $\mathcal{D}^2 = \mathbf{D} \cdot \mathbf{D}$.

We enforce the incompressibility condition by introducing a streamfunction $\Psi(\mathbf{x}, t)$ via $\mathbf{v}_{i,j} = \mathbf{D} \times (\Psi_{i,j} \hat{\mathbf{z}})$, and eliminate the pressure by taking the curl of Eqn. A9:

$$0 = -\eta \mathcal{D}^4 \Psi_{i,j} + (\mathbf{D} \times \mathbf{f}_{i,j}) \cdot \hat{\mathbf{z}}. \quad (\text{A11})$$

This equation can then be solved using fast Fourier transforms (FFT) with a computational cost that scales as $N_y N_x \ln(N_x N_y)$.

The discrete FT is defined as

$$\hat{\phi}_{k_x, k_y} = \sum_{i=0}^{N_x-1} \sum_{j=0}^{N_y-1} e^{-i(2\pi/N_x)ik_x} e^{-i(2\pi/N_y)jk_y} \phi_{i,j}. \quad (\text{A12})$$

The FT of Eqn. A11 is:

$$0 = -\eta \frac{16}{dx^4} \left[\sin^2 \left(\frac{\pi k_x}{N_x} \right) + \sin^2 \left(\frac{\pi k_y}{N_y} \right) \right]^2 \hat{\Psi}_{k_x, k_y} + \hat{\mathcal{F}}_{k_x, k_y}, \quad (\text{A13})$$

where $\hat{\Psi}_{k_x, k_y}$ and $\hat{\mathcal{F}}_{k_x, k_y}$ are the FTs of $\Psi_{i,j}$ and $(\mathbf{D} \times \mathbf{f}_{i,j}) \cdot \hat{\mathbf{z}}$ respectively. For any source force field $\mathbf{f}_{i,j}$, this equation is solved to find the FFT of the stream function, $\hat{\Psi}_{k_x, k_y}$. Via the inverse FFT, we find finally the streamfunction $\Psi_{i,j}$ and fluid velocity $v_{i,j}$ on the Eulerian mesh.

We define by $\alpha \equiv \Delta s/dx$ the ratio of the parameter Δs , which we recall sets the separation of Lagrangian mesh points, and the mesh size dx of the Eulerian grid. The value of this parameter is important to the effectiveness

of any immersed boundary simulation. Too large a value will lead to fluid leakage across the particle boundaries [52]. Too small a value leads to an increased computational effort. Throughout we use a value $\alpha = 1.42$.

b. Eulerian to Lagrangian velocity mapping

The discretized velocity field $\mathbf{v}_{i,j}$ as calculated on the Eulerian mesh in the previous substep is now interpolated to the Lagrangian particle boundary and wall nodes using the formula:

$$\mathbf{V}_s = \sum_{i=0}^{N_x-1} \sum_{j=0}^{N_y-1} \mathbf{v}_{i,j} \delta_h(\mathbf{x}_{i,j} - \mathbf{X}_s) dx^2. \quad (\text{A14})$$

Here we use a smoothed discretized delta function $\delta_h(\mathbf{x}) = \delta_h(x)\delta_h(y)$ [53] in which:

$$\delta_h(x) = \begin{cases} \frac{3}{8} + \frac{\pi}{32} - \frac{x^2}{4}, & \text{for } 0 < \frac{|x|}{dx} \leq 0.5 \\ \frac{1}{4} + \frac{1-|x|}{8} \sqrt{-2+8|x|-4x^2} \\ -\frac{1}{8} \arcsin(\sqrt{2}(|x|-1)), & \text{for } 0.5 < \frac{|x|}{dx} \leq 1.5 \\ \frac{17}{16} - \frac{\pi}{64} - \frac{3|x|}{4} + \frac{x^2}{8} \\ + \frac{|x|-2}{16} \sqrt{-14+16|x|-4x^2} \\ + \frac{1}{16} \arcsin(\sqrt{2}(|x|-2)), & \text{for } 1.5 < \frac{|x|}{dx} \leq 2.5 \\ 0, & \text{for } \frac{|x|}{dx} > 2.5. \end{cases} \quad (\text{A15})$$

c. Lagrangian dynamics of the particle boundary nodes

Given the Lagrangian velocities of the particle boundary nodes as just calculated, their positions can in principle be updated from timestep $n \rightarrow n+1$ simply by using an explicit Euler algorithm:

$$\mathbf{X}_s^{n+1} = \mathbf{X}_s^n + \Delta t \mathbf{V}_s. \quad (\text{A16})$$

For clarity, we omit here any particle number label p from \mathbf{X}_s , and include only node label s .

With such an update, the area of each particle should in principle remain constant due to the incompressibility of Stokes flow. In practice, however, using the raw \mathbf{V}_s in Eqn. A16 gives a small error in particle area conservation due to fluid leakage across the particle boundary. Over an entire simulation this was about 1% in the worst case. To correct for this, we used the following method [54].

Strict particle area conservation requires that over the area Ω and boundary $\partial\Omega$ of each particle:

$$\int_{\Omega} \nabla \cdot \mathbf{v} dA = \int_{\partial\Omega} \mathbf{v} \cdot \mathbf{n} dS = 0, \quad (\text{A17})$$

where we have used the divergence theorem in writing the first equality. In discretized form this reads:

$$0 = \sum_{s=0}^{N_s-1} \mathbf{V}_s \cdot \hat{\mathbf{n}}_s \Delta S_s, \quad (\text{A18})$$

with $\hat{\mathbf{n}}_s = \mathbf{n}_s/|\mathbf{n}_s|$, $\mathbf{n}_s = (Y_{s-1} - Y_{s+1}, X_{s+1} - X_{s-1}, 0)^T$, and $\Delta S_s = |\mathbf{n}_s|/2.0$. To enforce this constraint we define

$$M = \sum_{s=0}^{N_s-1} \mathbf{V}_s \cdot \hat{\mathbf{n}}_s \Delta S_s / \sum_{s=0}^{N_s-1} \Delta S_s, \quad (\text{A19})$$

and subtract this mean value from the normal velocity of any particle boundary node:

$$\mathbf{V}_s \rightarrow \mathbf{V}_s - M \hat{\mathbf{n}}_s. \quad (\text{A20})$$

We use this corrected velocity in the explicit Euler update. With this, the worst case variation in any particle area over a full simulation is smaller than 0.1%.

Given the updated \mathbf{X}_s round the boundary of each particle, the elastic boundary forces $\mathbf{F}_s^{\text{elastic}}$ are then recalculated using Eqn. A4. (In this, recall that the value

of the equilibrium internode length Δs is a constant and equal to its value as at the start of the shearing simulation.)

The nodes of different particles also interact via a truncated LJ force \mathbf{F}_s^{LJ} of the same general form as in Eqn. A2. They also interact with the wall nodes in the same way. The potential used is now of slightly softer form, however, with

$$E^{\text{LJ}}(\{\mathbf{X}_i\}) = 4K_{\text{LJ}} \sum_{s,s' < s} \left(3 \left(\frac{\sigma}{X_{ss'}} \right)^8 - 4 \left(\frac{\sigma}{X_{ss'}} \right)^6 \right). \quad (\text{A21})$$

The total force on any particle boundary node is then $\mathbf{F}_s = \mathbf{F}_s^{\text{elastic}} + \mathbf{F}_s^{\text{LJ}}$.

d. Lagrangian dynamics of the wall nodes

To effect a relative shearing motion of the walls under conditions of a constant imposed shear stress, any node s of the upper wall is tethered at any time t in the simulation via a strong spring force to a desired moving position $\mathbf{X}_s^{\text{upper}}(0) + \hat{\mathbf{x}} \int_0^t dt \hat{V}^{\text{upper}}(t)$, where $\mathbf{X}_s^{\text{upper}}(0)$ was that node's initial location. Accordingly we have:

$$\mathbf{F}_s^{\text{tether,upper}}(t) = -K_w \left[\mathbf{X}_s^{\text{upper}}(t) - \left(\mathbf{X}_s^{\text{upper}}(0) + \hat{\mathbf{x}} \int_0^t dt' \hat{V}^{\text{upper}}(t') \right) \right]. \quad (\text{A22})$$

Here $\hat{V}^{\text{upper}}(t)$ is the time-dependent rightward speed of the upper wall that must obtain (along with a counterpart leftward speed $\hat{V}^{\text{lower}}(t)$ for the lower wall, described below) in order to maintain a constant imposed shear stress in the soft particle suspension between the walls. Our aim in what follows is to calculate these required wall speeds. Averaging Eqn. A22 across all nodes in the upper wall, and denoting the average by an overbar, gives:

$$L_x \sigma \hat{\mathbf{x}} + \frac{L_x}{L_y - H} \eta (\hat{V}^{\text{upper}} + \hat{V}^{\text{lower}}) \hat{\mathbf{x}} + G^{\text{upper}} \hat{\mathbf{y}} = -K_w \left[\bar{\mathbf{X}}_s^{\text{upper}}(t) - \left(\bar{\mathbf{X}}_s^{\text{upper}}(0) + \hat{\mathbf{x}} \int_0^t dt \hat{V}^{\text{upper}}(t) \right) \right]. \quad (\text{A23})$$

The terms on the LHS arise from area-integrating the force balance condition over a rectangle of length L_x that entirely encloses the upper wall. (Recall that force balance states that the divergence of the stress tensor, plus any body forces, must everywhere equal zero.) Converting this area integral to a surface integral via the divergence theorem then gives terms arising from the integral of the shear stress separately along the upper and lower boundaries of that rectangle. The integrals along the side walls of the rectangle cancel by virtue of the periodic boundary conditions. The upper boundary of the rectangle lies in the solvent outside the walls, with the term in η giving the known shear stress in that Newtonian linear shear profile. (Here we have assumed that the semi-circular wall bumps, which are small on the scale of the channel height $L_y - H$, have negligible effect on the known result for the shear stress for Newtonian flow between flat parallel walls.) The lower boundary lies in the soft particle packing between the walls. Here we define σ to be the x -averaged shear stress in that packing, which must be independent of y across the packing.

Taking the time-derivative of the previous two equations gives respectively:

$$\dot{\mathbf{F}}_s^{\text{tether,upper}}(t) = -K_w \left[\mathbf{V}_s^{\text{upper}}(t) - \hat{\mathbf{x}} \dot{V}^{\text{upper}}(t) \right], \quad (\text{A24})$$

and (writing now only the x component):

$$\frac{L_x \eta (\dot{V}^{\text{upper}} + \dot{V}^{\text{lower}})}{L_y - H} = -K_w \left[\bar{V}_x^{\text{upper}}(t) - \dot{V}^{\text{upper}}(t) \right]. \quad (\text{A25})$$

Note that the time-derivative of the shear stress σ across

the packing, which would appear in Eqn. A25, is zero in

this constant-stress simulation.

Exactly corresponding counterparts to Eqns. A22 to A25 can then be written for the lower wall.

Given the Lagrangian velocities \mathbf{V}_s of the wall nodes as calculated in step 2 above, and their x -components averaged separately along the upper and lower walls, $\bar{V}_x^{\text{upper}}(t)$ and $\bar{V}_x^{\text{lower}}(t)$, Eqn. A25 and its counterpart for the lower wall form two coupled ordinary differential equations in the wall speeds, $\hat{V}^{\text{upper}}(t)$ and $\hat{V}^{\text{lower}}(t)$, that must be imposed to maintain a constant shear stress within the suspension. We update these imposed wall speeds by stepping these ODEs via the explicit Euler algorithm with timestep Δt .

These updated imposed wall speeds $\hat{V}^{\text{upper}}(t)$ and $\hat{V}^{\text{lower}}(t)$, together with the wall node velocities \mathbf{V}_s as calculated in step 2, are then substituted into Eqn. A24 and its counterpart for the lower wall, which are used to update the tether forces $\mathbf{F}_s^{\text{tether}}$ on the wall nodes, again using the explicit Euler algorithm with a timestep Δt .

The velocities \mathbf{V}_s of the wall nodes are also used to update the positions of the wall nodes. In principle, we should perform the update using the velocity of each node separately: $\mathbf{X}_s^{n+1} = \mathbf{X}_s^n + \Delta t \mathbf{V}_s$. However, over the course of a simulation this can lead to a small deforma-

tion in the shape of each wall. We therefore instead use the average node velocity for each wall. Therefore, for all nodes in the upper wall we compute

$$\mathbf{X}_s^{n+1} = \mathbf{X}_s^n + \Delta t \bar{\mathbf{V}}_s^{\text{upper}}, \quad (\text{A26})$$

with a corresponding expression for the lower wall.

e. Lagrangian to Eulerian force mapping

The Lagrangian forces on the particle boundary and wall nodes are finally mapped onto the Eulerian mesh. For any particle or either wall we perform the sum:

$$\mathbf{f}_{i,j} = \sum_{s=0}^{N_s-1} \mathbf{F}_s \delta_h(\mathbf{x}_{i,j} - \mathbf{X}_s) \Delta s, \quad (\text{A27})$$

(with N_s replaced by N_w for the walls), further summing over all particles and both walls. Here we use the same discretized delta function as adopted above in mapping the Eulerian velocities to the Lagrangian nodes.

-
- [1] J. R. Seth, L. Mohan, C. Locatelli-Champagne, M. Cloitre, and R. T. Bonnecaze, *Nature Materials* **10**, 838 (2011).
- [2] S. Cohen-Addad and R. Höhler, *Current Opinion in Colloid & Interface Science* **19**, 536 (2014).
- [3] S. Fujii and W. Richtering, *The European Physical Journal E* **19**, 139 (2006).
- [4] M. Cloitre and D. Vlassopoulos, *Applied Polymer Rheology*, 209 (2011).
- [5] D. Vlassopoulos and G. Fytas, in *High Solid Dispersions* (Springer, 2009) pp. 1–54.
- [6] T. Divoux, C. Barentin, and S. Manneville, *Soft Matter* **7**, 8409 (2011).
- [7] D. Bonn, M. M. Denn, L. Berthier, T. Divoux, and S. Manneville, *Reviews of Modern Physics* **89**, 035005 (2017).
- [8] T. Divoux, D. Tamarii, C. Barentin, S. Teitel, and S. Manneville, *Soft Matter* **8**, 4151 (2012).
- [9] M. Cloitre and R. T. Bonnecaze, *Rheologica Acta* **56**, 283 (2017).
- [10] H. A. Barnes, *Journal of Non-Newtonian Fluid Mechanics* **56**, 221 (1995).
- [11] G. Vinogradov, G. Froishteter, K. Trilisky, and E. Smorodinsky, *Rheologica Acta* **14**, 765 (1975).
- [12] G. Vinogradov, G. Froishteter, and K. Trilisky, *Rheologica Acta* **17**, 156 (1978).
- [13] C. J. Dimitriou and G. H. McKinley, *Soft Matter* **10**, 6619 (2014).
- [14] S. P. Meeker, R. T. Bonnecaze, and M. Cloitre, *Journal of Rheology* **48**, 1295 (2004).
- [15] D. D. Joseph, R. Bai, K. Chen, and Y. Y. Renardy, *Annual Review of Fluid Mechanics* **29**, 65 (1997).
- [16] J. R. Stokes, M. W. Boehm, and S. K. Baier, *Current Opinion in Colloid & Interface Science* **18**, 349 (2013).
- [17] S. Roman, A. Merlo, P. Duru, F. Risso, and S. Lorthois, *Biomicrofluidics* **10**, 034103 (2016).
- [18] A. Yoshimura and R. K. Prud'homme, *Journal of Rheology* **32**, 53 (1988).
- [19] S. P. Meeker, R. T. Bonnecaze, and M. Cloitre, *Physical Review Letters* **92**, 198302 (2004).
- [20] J. R. Seth, C. Locatelli-Champagne, F. Monti, R. T. Bonnecaze, and M. Cloitre, *Soft Matter* **8**, 140 (2012).
- [21] A. Poumaere, M. Moyers-González, C. Castelain, and T. Burghlea, *Journal of Non-Newtonian Fluid Mechanics* **205**, 28 (2014).
- [22] J.-B. Salmon, L. Bécu, S. Manneville, and A. Colin, *The European Physical Journal E* **10**, 209 (2003).
- [23] V. Mansard, L. Bocquet, and A. Colin, *Soft Matter* **10**, 6984 (2014).
- [24] B. Geraud, L. Bocquet, and C. Barentin, *The European Physical Journal E* **36**, 30 (2013).
- [25] T. Divoux, V. Lapeyre, V. Ravaine, and S. Manneville, *Physical Review E* **92**, 060301 (2015).
- [26] X. Zhang, E. Lorenceau, P. Basset, T. Bourouina, F. Rouyer, J. Goyon, and P. Coussot, *Physical Review Letters* **119**, 208004 (2017).
- [27] X. Zhang, E. Lorenceau, T. Bourouina, P. Basset, T. Oerther, M. Ferrari, F. Rouyer, J. Goyon, and P. Coussot, *Journal of Rheology* **62**, 1495 (2018).
- [28] T. Divoux, D. Tamarii, C. Barentin, and S. Manneville, *Physical Review Letters* **104**, 208301 (2010).
- [29] V. Grenard, T. Divoux, N. Taberlet, and S. Manneville, *Soft Matter* **10**, 1555 (2014).
- [30] T. Gibaud, C. Barentin, N. Taberlet, and S. Manneville, *Soft Matter* **5**, 3026 (2009).

- [31] T. Gibaud, D. Frelat, and S. Manneville, *Soft Matter* **6**, 3482 (2010).
- [32] T. Gibaud, C. Barentin, and S. Manneville, *Physical Review Letters* **101**, 258302 (2008).
- [33] A. Kurokawa, V. Vidal, K. Kurita, T. Divoux, and S. Manneville, *Soft Matter* **11**, 9026 (2015).
- [34] C. Perge, N. Taberlet, T. Gibaud, and S. Manneville, *Journal of Rheology* **58**, 1331 (2014).
- [35] J. Goyon, A. Colin, G. Ovarlez, A. Ajdari, and L. Bocquet, *Nature* **454**, 84 (2008).
- [36] G. Davies and J. Stokes, *Journal of Non-Newtonian Fluid Mechanics* **148**, 73 (2008).
- [37] A. Nicolas and J.-L. Barrat, *Faraday Discuss.* **167**, 567 (2013).
- [38] J. R. Seth, M. Cloitre, and R. T. Bonnecaze, *Journal of Rheology* **52**, 1241 (2008).
- [39] M. Christel, R. Yahya, M. Albert, and B. A. Antoine, *Soft Matter* **8**, 7365 (2012).
- [40] H. K. Chan and A. Mohraz, *Rheologica Acta* **52**, 383 (2013).
- [41] C. S. Peskin, *Acta Numerica* **11**, 479 (2002).
- [42] Any steady state quantity reported in this work is averaged in each run between the time t_{ss} at which it visibly attains a steady state, and $t_{ss} + \Delta t$ where $\Delta t \geq 500.0$. Each is further averaged over at least two independent simulations. The error bars then correspond to the standard error in the distribution of the time-series averages across these independent simulations.
- [43] L. Derzsi, D. Filippi, G. Mistura, M. Pierno, M. Lulli, M. Sbragaglia, M. Bernaschi, and P. Garstecki, *Physical Review E* **95**, 052602 (2017).
- [44] L. Derzsi, D. Filippi, M. Lulli, G. Mistura, M. Bernaschi, P. Garstecki, M. Sbragaglia, and M. Pierno, *Soft Matter* **14**, 1088 (2018).
- [45] We define the non-affine velocity $\mathbf{v}_{na}(x, y) = \frac{1}{\gamma_{bulk}H} [\mathbf{v}_{Euler}(x, y) - v_{fit}(y) \hat{\mathbf{x}}]$ and characterise the flow heterogeneity in the fluid bulk (over the reduced gap $y_{lower} + 5R < y' < y_{upper} - 5R$) as $\delta_{het} = \frac{\sqrt{\Lambda}}{\gamma_{bulk}H\sqrt{N_x N_{y'}}}$ with $\Lambda = \sum_{x, y'} [v_{Euler, x}(x, y') - v_{fit}(y')]^2$.
- [46] A. Lemaître and C. Caroli, *Physical Review Letters* **103**, 065501 (2009).
- [47] F. Pelusi, M. Sbragaglia, A. Scagliarini, M. Lulli, M. Bernaschi, and S. Succi, *Europhysics Letters* **127**, 34005 (2019).
- [48] S. Plimpton, *Journal of Computational Physics* **117**, 1 (1995).
- [49] W. C. Swope, H. C. Andersen, P. H. Berens, and K. R. Wilson, *Journal of Chemical Physics* **76**, 637 (1982).
- [50] <https://lammps.sandia.gov/>.
- [51] C. S. Peskin, *Acta Numerica* **11**, 479517 (2002).
- [52] Y. Bao, A. Donev, B. E. Griffith, D. M. McQueen, and C. S. Peskin, *Journal of Computational Physics* **347**, 183 (2017).
- [53] X. Yang, X. Zhang, Z. Li, and G.-W. He, *Journal of Computational Physics* **228**, 7821 (2009).
- [54] P. Newren, *Enhancing the immersed boundary method: stability, volume conservation and implicit solvers*, Ph.D. thesis, University of Utah (2007).